Chapter 4

$MnFe_2O_4$ nanoflower

Chapter 4: $MnFe_2O_4$ nanoflower

4.1. Introduction

In the past few years various strategies, which aim at enhancing the saturation magnetisation and anisotropy of the material have been suggested to improve the heating ability during MFH. It includes modifying the size, shape, structure and chemical composition of the IONPs [102], [106], [139], [165]. One specific structure, magnetic nanoflowers (MNFs) of iron oxide, is quite exciting as they have shown outstanding heating performance during both MFH as well as PTT [110], [132]. In addition, various other MNPs have been also evaluated and were found to display effective heating during MFH [166]. $MnFe_2O_4$ nanoparticles, in particular, have displayed heating and biocompatibility in line with IONPs [167]. It is believed that its heating performance could further be increased with nanoflower morphology as witnessed for iron oxide nanoflowers over iron oxide mono-core particles [131]. In the present work, highly-crystalline $MnFe_2O_4$ nanoflowers (MFs) was obtained through solvothermal reaction (Chapter 2, sec.2.2.2). The material, in addition to effective heating under an AMF, demonstrated impressive heating ability under NIR irradiation. The sample's structural and magnetic properties are systematically studied and correlated with their heating performance during MFH and PTT.

4.2. Results and discussion

The room temperature x-ray diffraction pattern obtained for MF nanoflowers is shown in *Figure 4.1a*. The pattern suggests the formation of single-phase material with the cubic crystal structure, Fd-3m space group. The peaks were observed at 18.3°, 30.1°, 35.4°, 37.1°, 43.1°, 53.4°, 56.9°, 62.5°, 70.9° and 73.8°, corresponding to planes (111), (220), (311), (222), (400), (422), (333), (440), (620) and (533) and were assigned to the crystallographic

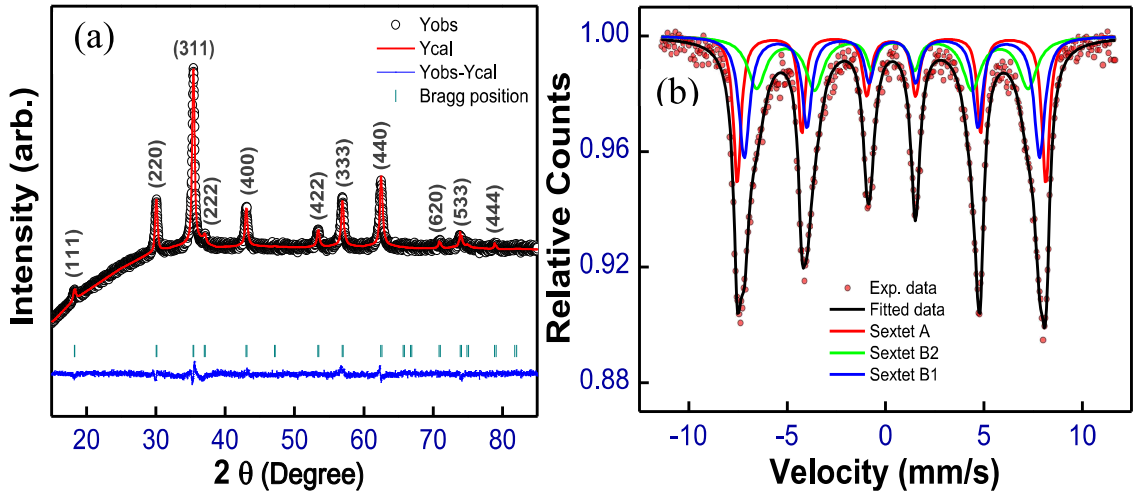

Figure 4. 1: (a) Rietveld refined XRD pattern and (b) room temperature Mössbauer spectrum of MF powder sample.

Table 4. 1: Parameters obtained from room temperature Mössbauer spectrum of powder MF sample.

Site	*Hyperfine field (H_f), T ± 0.01*	*Isomer shift (δ) mm/s ± 0.01*	*Quadruple splitting (Δ) mm/s ± 0.02*	*Outer line width (Γ) mm/s*	*Relative area (RA) ± 0.03%*	*X^2*
Sextet A	*48.63*	*0.286*	*0.019*	*0.470*	*29.70*	
Sextet B1	*46.53*	*0.328*	*-0.026*	*0.6598*	*37.96*	*1.21*
Sextet B2	*42.78*	*0.358*	*-0.039*	*1.104*	*32.31*	

planes of $MnFe_2O_4$, using reference JCPDS no 74-2403. Further, the pattern was refined using FullProf software. For the refinement, the initial site occupancy values were applied considering the structure $(Mn_{0.406}Fe_{0.594})[Mn_{0.594}Fe_{1.406}]O_4$, which was derived from Mossbauer spectroscopy (*Table 4.1*). The parameters defining the goodness of fit, i.e. R_{wp}, R_e and Chi^2, were converged to 13.5, 13.2 and 1.04, respectively, after the refinement. The lattice parameter (a=8.40 Å) obtained after Rietveld refinement was lower than that of the bulk sample (a=8.51 Å), which could be attributed to alternate cationic distribution leading to a different degree of inversion from the bulk [168]. The approximate crystallite size

calculated using Scherer's equation considering (311) peak was ~ 22 nm, which was higher than that obtained from the refinement (~ 19 nm). *Table 4.2* lists all the parameters obtained after the Rietveld refinement.

Table 4. 2: Summary of structural data of MF sample after Rietveld refinement.

Space group	a (Å)	V (A^3)	Density (g cm^{-3})	R_{wp}	R_e	X^2
Fd-3m	8.404	593.603	5.180	12.9	12.5	1.076
Atomic position	Fe1/Mn1 ($x = y = z$)				1/8	
	Fe2/Mn2 ($x = y = z$)				1/2	
	O ($x = y = z$)				0.2487	
Atom occupancy (site)						B_{iso}
	Fe1 (8a) Mn1 (8a)			0.609 0.394		0.12805
	Fe2 (16d) Mn2 (16d)			1.405 0.594		0.18108
	O (32e)			4		0.24787

The room temperature (300 K) Mössbauer spectrum obtained for sample MF without the application of an external field is shown in *Figure 4.1b*, and the corresponding parameters obtained after the least-square fitting of the experimental data are given in *Table 4.2*. Interestingly, a well resolved magnetically split absorption lines was noticed, which suggests that the particles were magnetically ordered and a ferri-magnetic like behaviour existed for the sample at RT [169]. The existence of only magnetically split lines in the spectrum also indicates that the blocking temperature of all the particles was higher than 300

K. The spectrum was well fitted with three Zeeman sextets, one for tetrahedral (A) and two for octahedral (B) sites [170]. The values of the isomer shift which were found between 0.2864 to 0.358 mm/s, suggest that all Fe ions were in Fe^{3+} high spin state [151], which was further supported from the findings of XPS spectroscopy (presented later). The sextet-A showing smaller isomer shift represents Fe^{3+} ions at A site, and it also exhibited the highest hyperfine field. The other two sextets, i.e. sextet B1 and B2 with relatively larger isomer shifts, characterise Fe^{3+} ions at two different environments in B-site [170], [171].

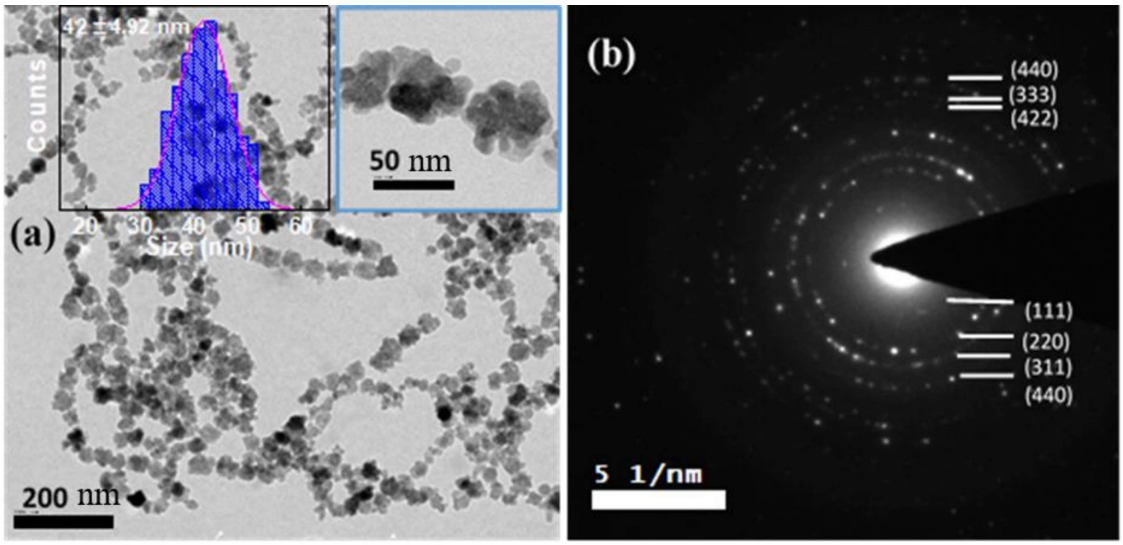

Figure 4. 2: (a) Bright-field TEM image (the insets show the size distribution profile and morphology at higher magnification) and (b) SAED pattern for MF sample.

The bright-field TEM micrograph depicts a chain-like arrangement for these nanoparticles (*Figure 4.2a*). The inset of the figure captured at higher magnification clearly shows the formation of a flower-like morphology. The smaller cores were adhered together to give the desired flower pattern. The average size of the flowers was observed to be ~42 nm with a standard deviation of 5 nm. The SAED pattern obtained was due to the planes of a spinel structure and indicates the formation of a crystalline structure, supporting the X-ray diffraction analysis.

The SEM-EDS spectrum confirmed the presence of Mn, Fe and O elements with atomic percentage of ~13, 24 and 63, respectively, in the sample. The SEM micrograph and the respective elemental mapping, acquired from the Kα energy of Mn, Fe and O, of the nanoflowers are represented in *Figure 4.3*. Thermo gravimetric analysis (TGA) was performed in 30 – 600 °C temperature range to estimate the amount of adsorbed chemical species on the nanoflowers obtained through solvothermal method as describe in chapter 2 (sec 2.2.2).

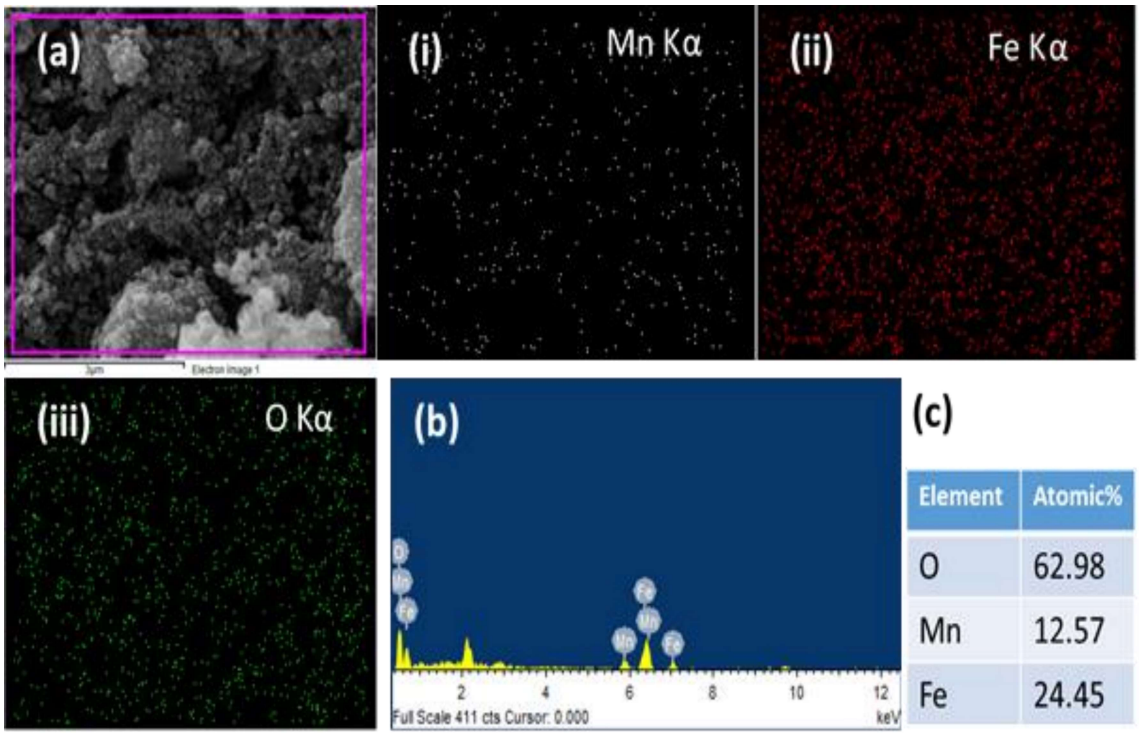

Figure 4. 3: (a) SEM-EDS elemental mapping for (i) Mn, (ii) Fe and (iii) O, (b) EDS spectrum and (c) elemental composition of MF powder sample.

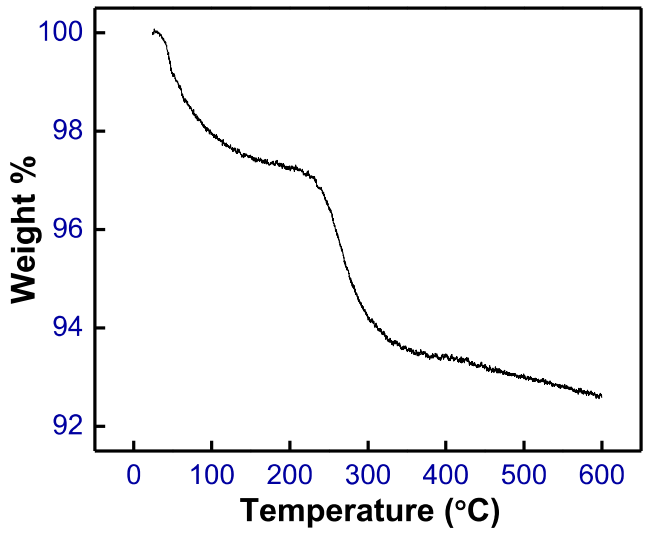

Figure 4. 4: TGA thermograph curve of MF powder sample.

The TGA curve (*Figure 4.4*) mainly revealed a two stage weight loss during the heating process. The first mass reduction, of ~3.0 %, started just above the initial measurement temperature to near 200 °C. This reduction might be associated with the evaporation of physically adsorbed water molecule and low boiling solvent complexes attached to the surface of nanoflowers [172], [173]. Above this temperature a further weight reduction of ~4.5% was noticed up to the measuring temperature of 600 °C. This could be due to the decomposition of chemically adsorbed species (solvent) and PVP [173]. Thus, overall a reduction of ~7.5% in weight was witnessed by TGA experimentation.

The XPS analysis of MF sample was performed in order to check the oxidation states of the elements present in the sample. The high-resolution XPS scans of Fe 2p, Mn2p, Fe3p, O1s and C1s are shown in *Figures 4.5 (a-e)*, respectively. The Fe 2p XPS spectrum was splitted into Fe $2p_{3/2}$ and Fe $2p_{1/2}$ orbitals having peaks at 711.20 and 724.56 eV, respectively, due to spin-orbit coupling. The spectrum displayed the existence of a satellite peak around 719.25 eV which was separated by 8.05 eV from the Fe $2p_{3/2}$ peak. These data suggest that

the Fe 2p spectrum was due to the Fe^{3+} ionic state [174], [175]. The oxidation state of Fe was also confirmed from the Fe 3p XPS spectrum. In a study, *Yamashita et al.* [174] had found the Fe 3p peak position at 55.6 eV (S.D=0.04) and 53.7 eV (S.D=0.03) for Fe^{3+} and Fe^{2+} states respectively. In the Fe 3p spectrum obtained for the MF sample, a peak around 55.2 eV was observed, which could be due to the Fe^{3+} ionic state. The absence of any peak around 53.7 eV in the spectrum suggests that only Fe^{3+} ions were present in the sample. Further, the Fe 2p XPS spectrum was de-convoluted with the help of five sub-peaks. The peaks at 710.9 (724.23) eV and 713.4 (726.5) eV were assigned to Fe^{3+} from octahedral (o) and tetrahedral (t) sub-lattices respectively [176], [177].

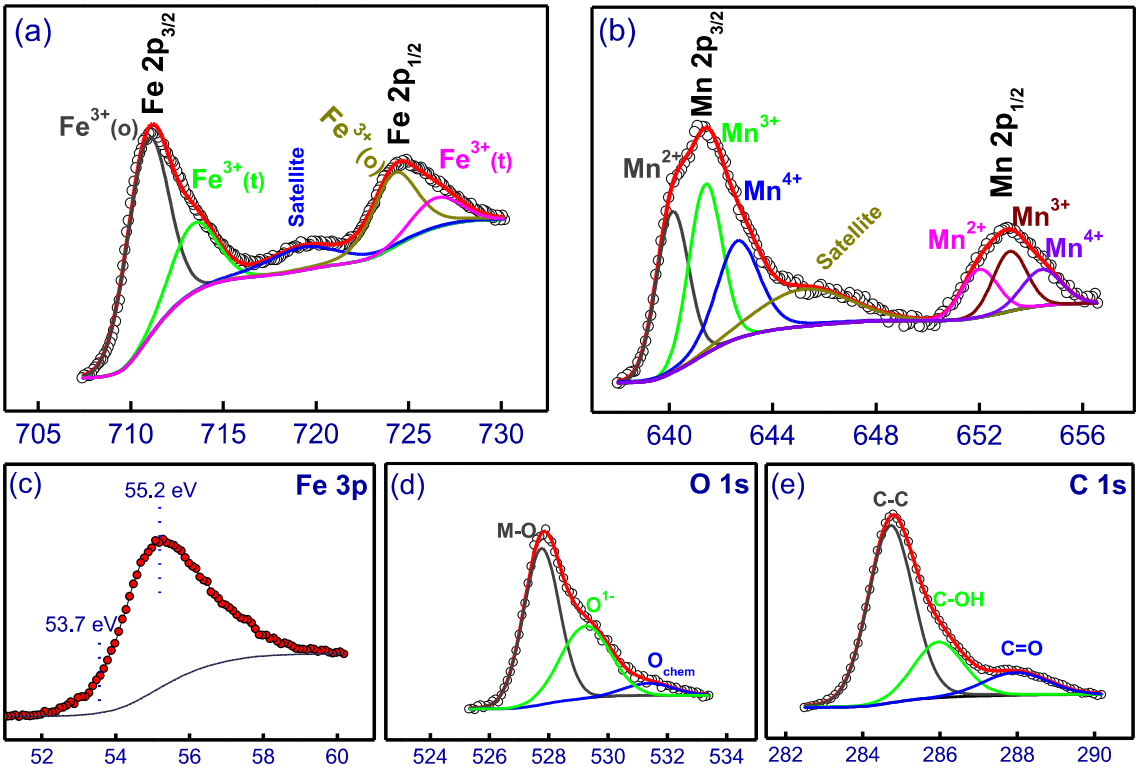

Figure 4. 5: High-resolution XPS spectra for (a) Fe 2p, (b) Mn 2p, (c) Fe 3p, (d) O 1s and (e) C 1s core-levels of MF powder sample.

The Mn 2p XPS spectrum for the sample indicates the presence of a multivalent ionic state for Mn. The peaks at 640.12 (652) eV, 641.4 (653.18) eV and 642.64 (654.4) eV were assigned to Mn^{2+}, Mn^{3+} and Mn^{4+} ionic states respectively [178], [179]. The XPS spectrum for O 1s was de-convoluted with three peaks positioned at 529.75, 531.24, and 533.35 eV, which corresponded to metal ions oxygen bonds, surface-adsorbed oxy-hydroxide and chemically adsorbed H_2O at the surface, respectively [179].

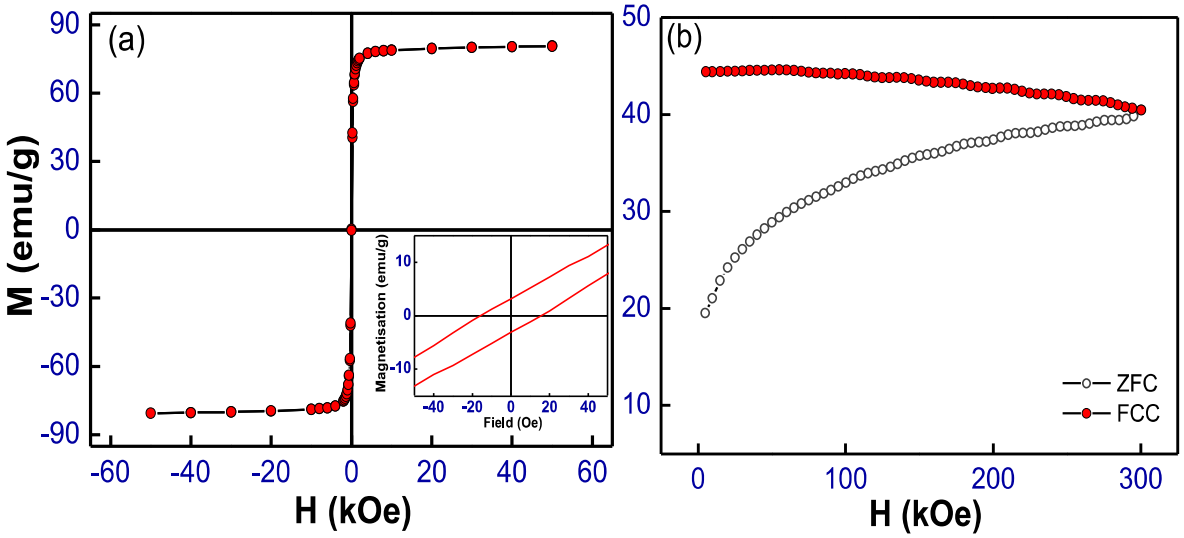

Figure 4. 6: (a) Room temperature magnetisation vs. field curve and (b) temperature dependent (5 – 300 K) magnetic behaviour (ZFC-FC) for powder MF sample.

Figure 4.6a and *b* show the hysteresis loop recorded up to ± 50 kOe at 300 K and a temperature-dependent magnetization behaviour from 5K-300K, measured under ZFC and FC conditions at a static magnetic field of 250 Oe, respectively. As apparent from the room temperature DC magnetometry M-H curve (*Figure 4.6a*), an early saturation in magnetization was attained for these nanoflowers. The saturation magnetization (M_S) value was observed to be ~80 emu/g for MF, which was close to the bulk magnetization value (~83 emu/g) for $MnFe_2O_4$ [168]. The high M_S value could be due to the reduced surface disorder and an enhanced magnetic ordering within the nanoflowers, a constructive aspect of such a

structure. This could be appreciated from the reported M_S values for single-core nanoparticles of comparable sizes, which were relatively lower than for the present nanoflower [168], [170]. The sample displayed a finite coercive field (H_C) of ~15 Oe and remanent magnetization (M_r) of ~3.2 emu/g as depicted from the inset of *Figure 4.6a*.

The temperature-dependent magnetisation behaviour (5 – 300 K) for MF in ZFC and FC condition with an applied field of 250 Oe displayed remarkable magnetic behaviour (*Figure 4.6b*). The curves showed an irreversible behaviour right from 300 K down to the lowest measurement temperature of 5 K. The irreversibility, or in other words, the bifurcation between the ZFC and FC curves was getting larger on decreasing the temperature, which, directs to the presence of higher magnetic anisotropy field. The ZFC curve displayed a continuous increase in magnetisation on increasing the experimental temperature from 5 to 300 K. The absence of any peak in the ZFC magnetisation curve indicates that the particles were essentially in the magnetically blocked condition up to room temperature, supporting the findings of Mössbauer spectroscopy [169]. The FC curve depicts a typical characteristic of material with strong magnetic inter-particle or dipole-dipole interaction. This interaction may be the reason for the chain-like assembly observed in bright-field TEM micrograph (*Figure 4.2a*). Such an interaction, depending on the characteristics of an individual particle and the AMF parameters, can either enhance or impair the MFH performance [46], [155]. In clusters of nanoflowers, the existence of supraferromagnetic interaction enhances the heating performance during MFH [112].

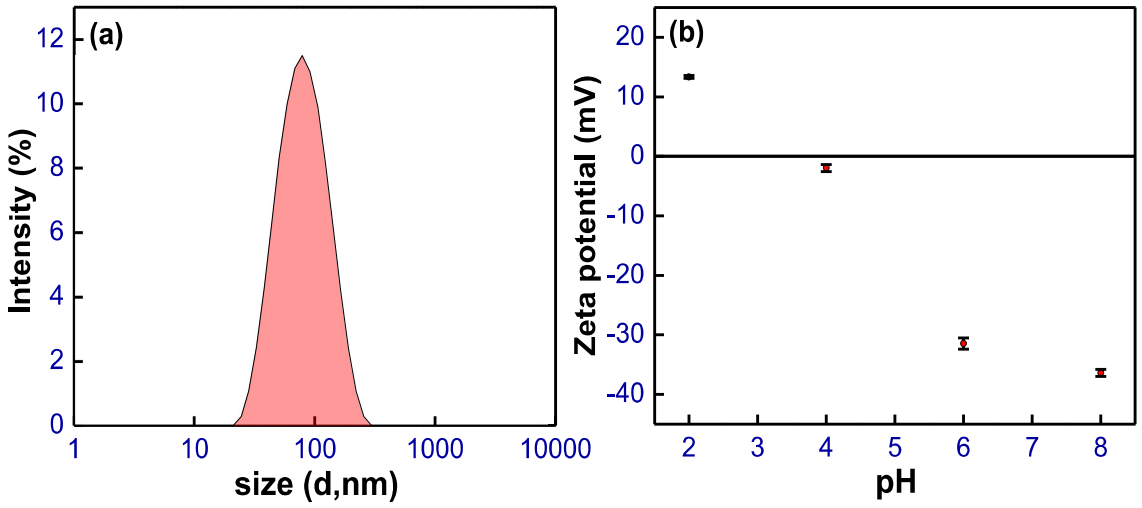

Figure 4. 7: (a) DLS – hydrodynamic size profile and (b) pH dependent zeta-potential of particles in aqueous ferrofluid.

The aqueous ferrofluid showed good stability as observed from the zeta potential (ζ) measurement. The mean ζ values were quantified as 13.33 ± 0.25, -1.96 ± 0.58, -31.43 ± 0.95 and -36.67 ± 0.61 at 2, 4, 6 and 8 pH values, respectively (*Figure 4.7b*). The dynamic light scattering plot (*Figure 4.7a*) depicted a unimodal distribution of hydrodynamic size (D_h) for the MF particles dispersed in the aqueous medium. The mean D_h value was observed to be 81 ± 1.06, which was higher than the particle's size observed in TEM as expected, as the former display the hydrodynamic radius value.

Figure 4.8a shows an increase in temperature of aqueous ferrofluid of concentration 2 mg/mL after exposing it to AMF of different field intensities and frequencies. The temperature elevation curves were plotted by taking the average of three readings. As can be observed from the graph, the ferrofluid displayed a continuous rise in temperature but with dissimilar rates at different applied AMFs. For example, it took an average time of ~465 s to reach the therapeutic temperature (~42 °C) when exposed to an AMF of amplitude 110

Oe and frequency 466 kHz while the same has been achieved in only ~175 s at 170 Oe and 330 kHz.

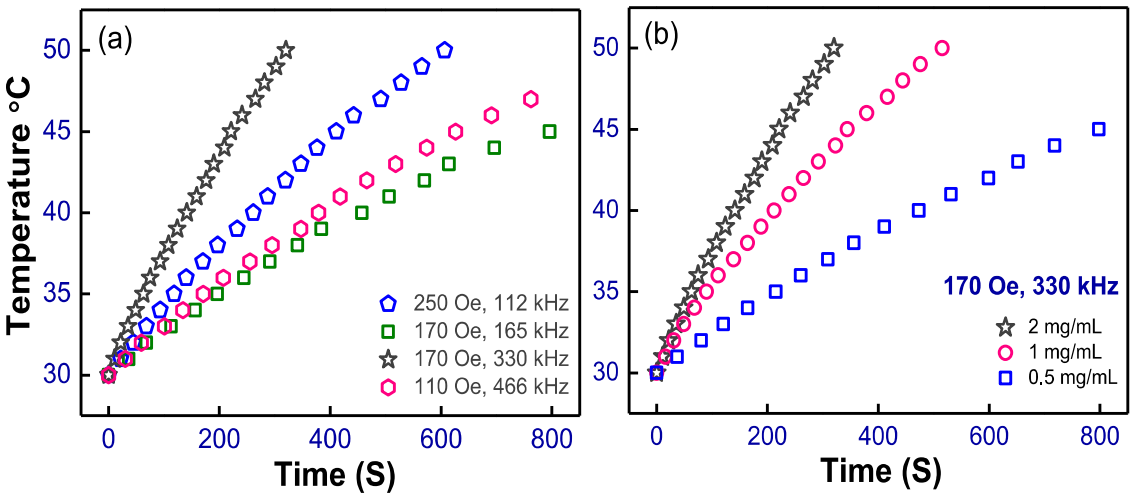

Figure 4. 8: (a) Field intensity and frequency dependent temperature rise curves with time for aqueous ferrofluids of concentration 2 mg/mL, and (b) concentration dependent temperature rise curves at the AMF of 170 Oe, 330 kHz.

The heating behaviour of magnetic nanoparticles is believed to vary with amplitude and frequency of applied AMF as H^2 (constant *f*) and *f* (constant H) in the regime of linear response theory [79]. But as witnessed from the temperature-dependent magnetisation behaviour, these nanoflowers were in a ferri-magnetically blocked state, so a deviation from a simple H^2 behaviour is likely to be expected [103]. Though with the limitation of the equipment used, it is not possible to evaluate the heating behaviour at the varying field with constant frequency and vice-versa, a qualitative evaluation is still possible. At the AMF of amplitude 170 Oe, the ILP value has increased from 2.62 ± 0.052 to 4.07 ± 0.061 nHm^2kg^{-1} by increasing the frequency of AMF from 165 to 330 kHz.

An increased frequency tends to enhance the M-H loop's hysteresis area during the dynamic magnetisation process, which is a direct measurement of heat dissipated

(temperature rise) during MFH [82]. The ILP value was 2.96 ± 0.06 and 2.56 ± 0.063 nHm^2kg^{-1} at 250 Oe, 112 kHz and 110 Oe, 466 kHz, respectively. While 250 Oe was the highest field intensity utilised in the experiment, the maximum in ILP was not achieved due to the lower field frequency associated with it. Again at the highest field frequency, 466 kHz, the associated field intensity was lowest (110 Oe), which might not be sufficient to rotate the maximum moment in its direction and hence lower heating was noticed [102], [103]. The heating behaviour could further be enhanced by increasing the magnitude of AMF, as the anisotropy field of the sample was higher (suggested by ZFC/FC magnetisation) than the field intensity used in the hyperthermia experiment. However, of all AMFs applied, the maximum heating of MF ferrofluid was observed at 170 Oe and 330 kHz, so further decided to evaluate a concentration-dependent heating behaviour at the same AMF. As the inter-particle and dipolar interactions are present in our sample, the heating behaviour is expected to vary with concentration [70], [103].

Figure 4.8b shows the temperature elevation profile of MF ferrofluid of different concentrations at 170 Oe and 330 kHz. As observed from the curves, the efficiency of heating improved at a lower concentration. The ferrofluid displayed the highest ILP of 5.70 ± 0.085 at the concentration of 1 mg/mL. However, it was lower than that of γ-Fe_2O_3 nanoflowers which demonstrated an ILP value of 15.21 ±0.34 nHm^2kg^{-1} at same AMF, but comparable to that of previously reported Fe_3O_4 nanoflowers [110]. The respective ILP values at the concentrations of 2 and 0.5 mg/mL were 4.07 ± 0.061 and 4.77 ± 0.057 nHm^2kg^{-1}, respectively. The observed variation in ILP of the ferrofluid could be explained through the effective anisotropy modified due to concentration variation. An increased concentration is associated with the enrichment of magnetic dipolar interactions and cluster formation, which

tend to increase the system's effective anisotropy [46], [155], [180]. Thus, the increased effective anisotropy might have restricted a more part of the magnetization reversal in the field direction at higher concentrations. It could lead to a decrease in area under the hysteresis lowering the heat output. In hyperthermia, the final aim of all modifications, such as shape, size, concentration or field and frequency, is to make the anisotropy of the material close to the amplitude of the field applied in order to maximize the heating behaviour [102], [103]. The concentration of 1 mg/mL might have provided the right condition and hence achieved maximum ILP. AC magnetometry experiments could further be used for the exact explanation of such behaviour.

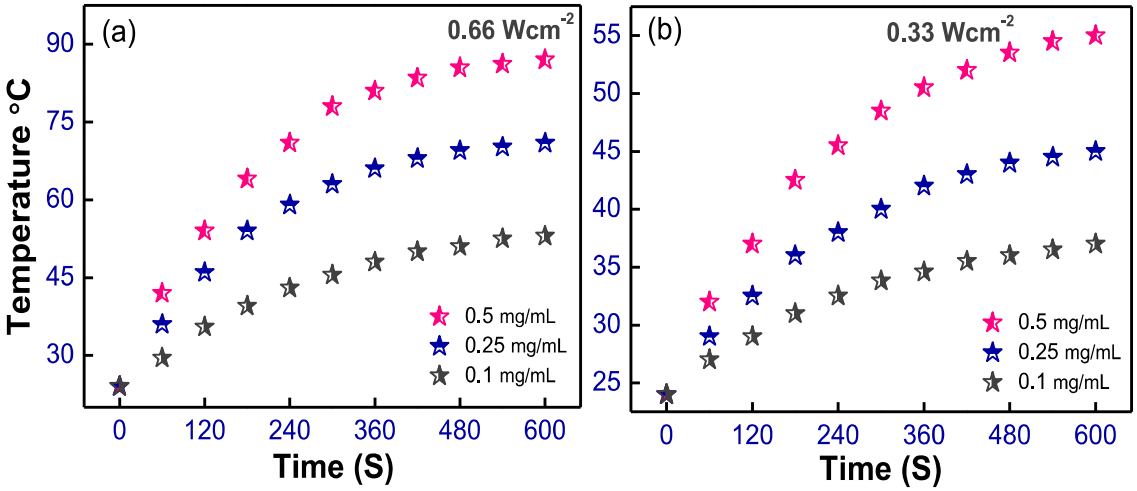

Figure 4. 9: Concentration dependent heating behaviour of aqueous suspension of MF when exposed to NIR laser of wavelength 808 nm of (a) 0.66 Wcm^{-2} and (b) 0.33 Wcm^{-2} power density.

The temperature elevation curves for aqueous suspension of MF of different concentrations when irradiated with NIR laser of wavelength 808 nm of power density 0.66 and 0.33 W/cm^2 are shown in *Figure 4.9a* and *b* respectively. The temperature rise was observed to be dependent on the concentration of the aqueous suspension and the power density of the NIR laser. For instance, after the exposure to the NIR of 0.66 W/cm^2 for 10

min, the temperature reached ~87, 71 and 53 °C (initial temperature was 19 °C) for the aqueous suspension of concentration 0.5, 0.25 and 0.1 mg of material per mL, respectively. The temperature achieved after NIR irradiation of aqueous suspension of concentration 0.5 mg/mL was higher than that achieved by applying AMF for the same period of time. Even with the higher concentration (i.e. 2 mg/mL) the temperature rose by ~20 °C after 5 min of AMF exposure, whereas a rise of ~55 °C in temperature was observed after NIR exposure over the same period of time with lower concentration. The specific loss power (SLP) was observed to be dependent on the concentration and decreased with increased concentration of aqueous suspension. For example, the SLP values obtained with 0.66 Wcm^{-2} power density for 0.5, 0.25 and 0.1 mg/mL aqueous suspension were ~2520, 3360 and 3864 Wgm^{-1}, respectively. The values further decreased to ~1117, 1344 and 2100 Wgm^{-1}, respectively, for 0.5, 0.25 and 0.1 mg/mL aqueous suspension by lowering the power density of the NIR laser light to 0.33 Wcm^{-2}. Overall, a better heating was witnessed with NIR laser irradiation and the maximum in SLP value was almost an order higher than that observed with AMF exposure (highest SLP ~320 Wgm^{-1}). The DI water under the same condition displayed a temperature rise of ~ 2 °C with 0.66 Wcm^{-2} power density, which confirms that the heating was essentially due to the MF particles. While, lowering the NIR laser's power density to 0.33 W/cm^2 resulted in a drop in the temperature achieved after the same period of exposure. At this power density, no obvious temperature increment (~1 °C) was observed for the DI water. It is well known that the non-radiative recombination of the electron hole-pair (during the relaxation from excited sate) is responsible for the generation of phonons which upsurge the vibrational state of the system leading to heat release and a subsequent temperature rise [19], [140]. The non-radiative recombination of electron-hole pair, generated during the excitation, could be increased by introducing the defect state in the material [140].

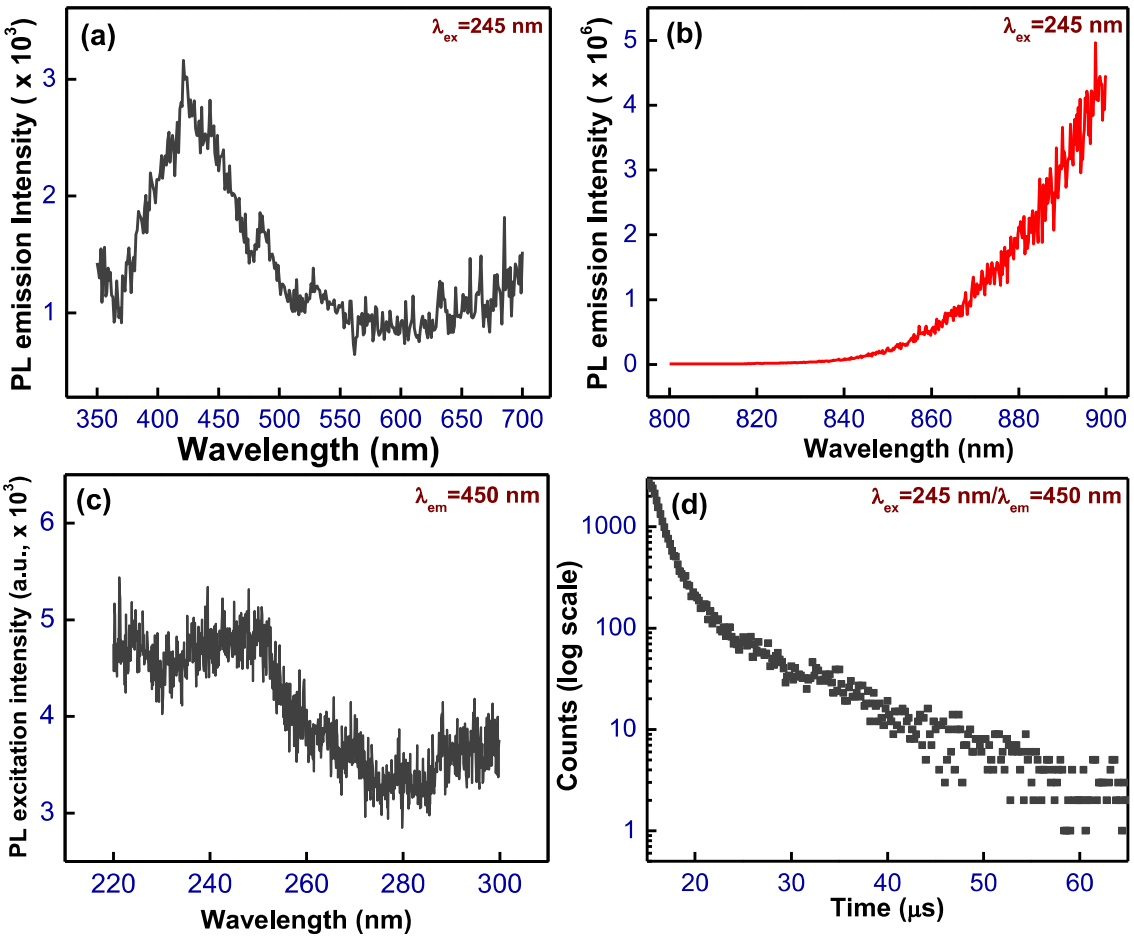

Figure 4. 10: (a) Emission (Visible range), (b) Emission (NIR range) (c) excitation and (d) lifetime spectra of aqueous suspension of MF sample.

Photoluminescence measurements are shown in *Figures 4.10*. The visible emission spectrum (*Figure 4.10a)* of nano-crystalline $MnFe_2O_4$ under 245 nm excitation showed a prominent broad peak at around 430 nm and two smaller peaks at around 480 and 530 nm. In addition, several feeble peaks could be observed over 600 to 700 nm. Such multiple peaks are ascribed to the presence of several defect states in the band-gap of nano-crystalline $MnFe_2O_4$. *Jacintha et al.* [181] have also observed multiple PL bands in the range 415-600 nm, and the same has been attributed to the presence of defects and oxygen vacancies (OVs). The OVs can be neutral, singly ionized or doubly ionized depending upon the formation energy [182], [183]. *Gupta et al* [182] have ascribed the blue bands at 423 and 483 nm to the

transition from the conduction band to the defect state created by the presence of neutral OVs. While several authors have attributed the presence of a blue band in PL spectrum of $MnFe_2O_4$ to the radiative defects associated with interface traps existing at the grain boundaries [161], [181], [184]. This conclusion was followed after *Jin et al* [185], who ascribed the violet luminescence at 420 nm to the radiative defects related to the interface traps existing at ZnO-ZnO grain boundaries. *Nguyen et al* [186] have attributed the PL peak at 425 nm for Fe_3O_4 to the radiative recombination of the trapped electron from the octahedral sites to O 2p level. In fact, *Nguyen et al.* [186] and *Sadat et al.* [140] could propose the band-gap structure of Fe_3O_4 from PL measurements.

In $MnFe_2O_4$, the substitution of $Fe^{2+/3+}$ ions at octahedral and tetrahedral sites by Mn^{2+}/Mn^{3+} ions are believed to modify the defect states and band structure. Here, a wide blue band centered around 430 nm (2.88 eV), suggests the presence of various defect states, could arise due to radiative recombination of trapped electrons at the octahedral site to the photo-generated holes from the O 2p state [186]. A green band at 530 nm (2.33 eV) could refer to the radiative recombination of mobile electrons from, e_g to t_{2g} at the octahedral site [140], [186]. In Fe_3O_4, the energy gap due to crystal field splitting at octahedral is ~ 2.2 eV [140]. In addition, a green band also appear due to radiative recombination of the photo-excited hole with electron trapped in singly ionized oxygen vacancies (F^+-centres) [161]. The feeble peaks observed over 600 to 700 nm (2.06-1.77 eV) could have stirred by the radiative recombination of trapped electrons from octahedral or crystal field (t_{2g}) on tetrahedral sites to the O 2p valence band [186].

NIR PL spectra of nanocrystalline MF altogether showed impressive results. Under 245 nm excitation, there is a progression of a very intense peak in the region of 800-900 nm

(*Figure 4.10b)* with a relative photon count of 106. The emission peak around ~870 nm can be attributed to the transitions of trapped electrons from one defect state to another in tetrahedral position. Sadat *et al.* [140] have observed NIR peak at around 840 nm in nano-crystalline Fe_3O_4 and ascribed the same to electron traps in oxygen vacancies (OVs) at the tetrahedral site. Due to the limitation of our instrument having a PMT detector that is sensitive up to 900 nm, further measurement was not possible. However, such an intense NIR peak is one reason for the excellent photo-thermal property of nano-crystalline MF.

The PL excitation spectrum (*Figure 4.10c*), on the other hand, displayed a band around 245 nm, which can have the combined contribution from intrinsic $O^{2-} \rightarrow Fe^{3+}$ charge transfer as well as transition involving defect state [160]. Such a peculiar band in the UV region is typical of spinels [187]. The lifetime of the defect induced blue band in nano-crystalline MF is around 8.23 µs as obtained by mono-exponential fitting of luminescence decay profile shown in *Figure 4.10d*. Such lifetime is typical of singly ionized OVs (also known as F^+ centers) found in spinels.

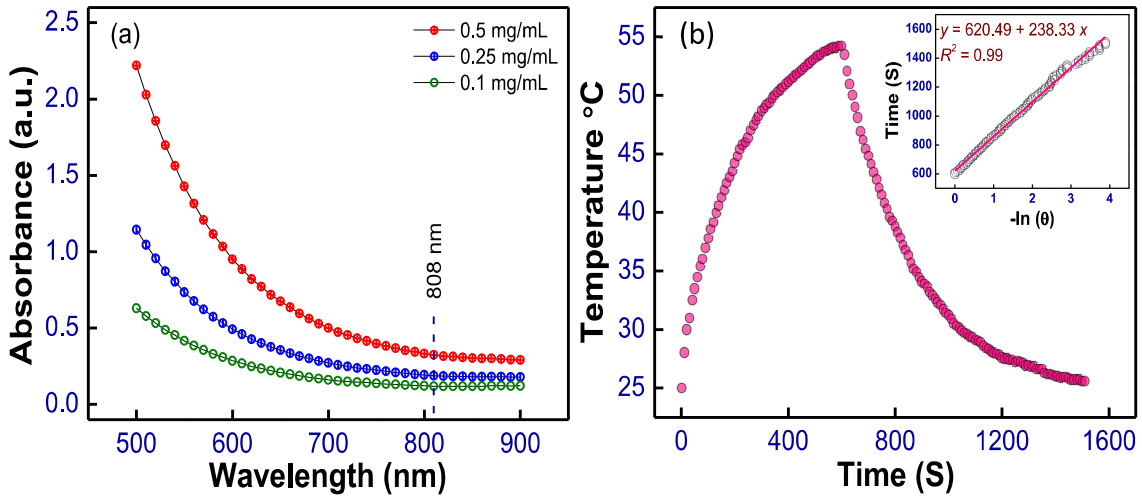

Figure 4. 11: (a) Concentration dependent UV-vis absorption spectra, and (b) heating and cooling curves for 0.5 mg/mL aqueous suspension under 0.33 Wcm^{-2} laser irradiation.

Figure 4.11a illustrates the concentration-dependent absorption behaviour for the aqueous MF suspension over a wavelength span of 500 to 900 nm. The suspensions displayed absorbance over the entire span, which decreased with increasing wavelength. In addition to the non-radiative relaxation process, the photo-thermal therapy is directly dependent on their NIR optical absorption efficiency. A finite absorbance near the NIR region, which was 0.324, 0.188 and 0.119 at concentration 0.5, 0.25 and 0.1 mg/mL, respectively, were observed for the suspension.

Figure 4.11b shows the time-dependent heating and cooling cycle for the aqueous suspension of MF (0.5 mg/mL) after exposure to 808 nm NIR of 0.33 Wcm^{-2} power density. A decay time of ~ 238 s was obtained from the analysis of the cooling cycle (inset Figure). The corresponding *hA* value was deduced to be 7.42 W/°C. The photo-thermal efficiency was found to be ~ 63 % using *equation 2.3* (chapter 2). In the previous work, this efficiency was found to be ~ 70 % for γ-Fe_2O_3 nanoflowers. Though the temperature achieved with MF was higher, its lower efficiency is due to its relatively higher absorbance at 808 nm. For IONPs with different coatings, *Sadat et al.*[140] had observed 'η' values ranging from ~16-76 %, which portray the suitability of these MNPs as an alternative photo-thermal agent.

4.3. Conclusion

The $MnFe_2O_4$ nanoflowers was successfully synthesised via solvothermal process and was confirmed from XRD, XPS, TEM and Mössbauer spectroscopy. The nanoflowers displayed improved saturation magnetisation owing to the reduced surface disorder and possible magnetic ordering within the flowers. The highest ILP value of 5.70 ± 0.085 nHm^2kg^{-1} observed at an AMF of amplitude 170 Oe and frequency 330 kHz is comparable to the values for Fe_3O_4 nanoflowers reported earlier. The material showed a very high heating

capability under NIR irradiation of low power density. The intense NIR photo-counts is one reason for its excellent photo-thermal performance. The aqueous suspension of the nanoflowers showed good absorbance near NIR region and a photo-thermal conversion efficiency of ~63%. Under NIR irradiation the therapeutic temperature (~42-46 °C) was achievable even at a low concentration of 0.1 mg/mL. It makes the current MF sample as a prospective photo-thermal agent.